Technical article

Advanced electromagnetic modeling applied to anti-vibration systems for high precision and automotive applications

Abstract — This paper presents the application of two (semi-)analytical modeling techniques to the design of anti-vibration systems. Both methods are based on the direct solution of the Laplace and Poisson equations in terms of the scalar or magnetic vector potential. The first technique, the surface charge model, is applied to the design of an electromagnetic gravity compensator for the high precision industry. The second technique, the harmonic model, is applied to the design of an electromagnetic active suspension system for the automotive industry. These techniques facilitate the electromagnetic analysis, numerical optimization and design for a broad range of topologies and configurations. Furthermore, prototypes of both anti-vibration systems are manufactured and extensive experimental tests have proven the analytical analysis and design.
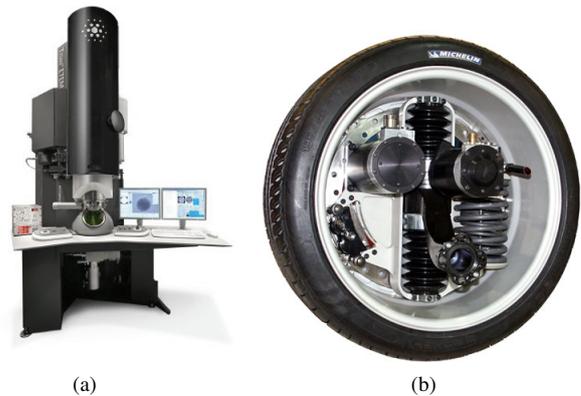
(a)   (b)

Fig. 1: Examples of applications that require vibration isolation are (a) microscopy (Courtesy of the FEI Company) and (b) in-wheel motors (Courtesy of Michelin).

I   INTRODUCTION

Vibrations of all sorts and kinds accompany us in our everyday life. Examples are the vibration of motors and machine tools, oil and gas platforms, buildings and constructions in a zone of seismic activity, undesirable vibrations of laboratory tables, setups, acoustic vibrations, microscopy or automotive applications such as those shown in Figs. 1(a) and 1(b). Very often these vibrations are undesired and as a result an object or platform is to be isolated from the source of the vibrations. Although varying in scale, complexity and performance the goals of the vibration isolation systems that accomplish this task are in essence identical: providing a sufficiently stable platform for the application that is envisaged. As such, the system must behave soft to floor vibrations, such that they do not transfer to the isolated platform. Simultaneously, is must behave as a hard spring to forces that act directly on the isolated platform in order to minimize their influence. These requirements are conflicting by nature and as a result a passive vibration isolation system is always a suboptimal compromise between them. Active systems are not limited to this strict rule and have therefore been used throughout the industry to improve the vibration isolation capabilities of such systems.

To date, vibration isolation systems often incorporate pneumatic devices in the high precision industry and hydraulic or pneumatic devices in the automotive industry. Although these systems are technologically relatively mature, they exhibit some major drawbacks such as their limited vibration isolation bandwidth and high energy consumption due to the necessity of a continuously pressurized system. Furthermore, high-precision systems often suffer from the difficulties to operate in a vacuum environment.

Electromagnetic systems offer excellent alternatives to overcome these drawbacks. Recent research at the Electromechanics and Power Electronics Group (EPE) at the Eindhoven University of Technology has resulted in two electromagnetic anti-vibration systems for the high precision industry [1] and automotive applications [2], respectively. This article presents an overview the extensive analytical modeling, optimization, design and experimental verification that have been performed in the light of this research. A common factor in both researches is the use of (semi-)analytical models to describe the electromechanical behavior of the considered devices. Section II provides argumentation for such advanced (semi-)analytical modeling. Section III describes an electromagnetic gravity compensator for the high-precision industry (Case A) and Section IV presents an electromagnetic active suspension system for automotive applications (Case B). Finally, Section V presents the conclusions.

II   ELECTROMAGNETIC MODELING TECHNIQUES

The ever increasing performance requirements of electromagnetic and electromechanical devices continue to demand improvements in the accuracy on which these devices are modeled. For instance, some devices require a 3D modeling approach or a dynamic modeling approach instead of a static model. Numerical models, such as Finite Element Analysis (FEA), are often used to accomplish such tasks as a result of their versatility and powerful solving capabilities. For each numerical method it holds that an increased mesh density improves the modeling accuracy until a point where numerical instability is reached. However this is at the cost of an increased computational time. Nevertheless, such numerical methods are generally considered to be the most generic approach to analyze electromagnetic problems as they are suitable to model most industrial components and systems with the least amount of assumptions. They have the ability to handle complex geometries, include non-linear material parameters and couple various physical domains, such as the magnetic/thermal, magnetic/mechanical or electrical/thermal ones [3]. Furthermore, the capability of analyzing transient phenomenon and the coupling with electrical circuits or power electronics made these methods very popular in research and engineering.

However, a correct geometry discretization requires prior knowledge of the field distribution to obtain a reliable solution.

In ironless structures without concentrated magnetic fields [4, 5] or machines with a small airgap or stroke compared to their dimensions [1], these numerical methods become even more problematic due to the necessity of a large number of discrete mesh elements. Therefore, (semi-)analytical methods are often used during the design proces of such devices whereas FEA is generally used as a verification method. Although these techniques have some additional modeling assumptions, the design process remains significantly faster as a result of their lower computational requirements.

To obtain an accurate field solution independent on the geometrical sizes without the necessity of prior knowledge, the so called direct solution of the magnetic field equations is considered in this article. For the magnetostatic case, the Maxwell equations can be written in terms of the scalar or magnetic vector potential, reducing the set of equations to a Laplace or Poisson equation. The solution of these partial differential equations (PDE) can be obtained using Green's functions or separations of variables, depending on the description of the source terms (permanent magnets and current densities) and the boundary value problem. An example which uses Green's functions to describe the field solution is the surface charge modeling technique for permanent magnets in free space. The other variant is the so called harmonic modeling technique, in which the source terms and field solution are written in terms of Fourier series, especially applicable to periodic problems.

Each of the modeling techniques has their own advantages and disadvantages and it strongly depends upon the application which one is preferable. This work will present the application of each of the modeling techniques to the design of an anti-vibration system for high precision applications (Case A) and automotive applications (Case B).

III CASE A: GRAVITY COMPENSATOR FOR HIGH PRECISION APPLICATIONS

Today, an increasing number of high-precision applications requires a platform or table which is extremely well isolated from vibrations [6]. They demand a stable environment to function at their peak of accuracy and precision. The influence of typical disturbances like ground motions, personnel activities and the extensive support machinery on the isolated system needs to be reduced. A well-designed isolation system relaxes the requirements on the floor or the building in which it is placed. Examples of extremely vibration-sensitive instruments are found in facilities such as those for metrology systems, microbiological research, optical research, space research or in the chip manufacturing industry [7, 8].

Typical to these applications are the small amplitudes and high frequencies of the floor vibration that need to be isolated. Further, the systems that are isolated are often heavy, mechanically stiff platforms which should be isolated from disturbances along six degrees of freedom (DoF), as summarized in Table 1. Therefore, most advanced vibration isolation systems that are seen today employ a single 6-DoF gravity compensator that exhibits a large vertical force with an extremely low position dependency, or stiffness. As the pre-compression and leveling of such device may become a problem (in the order of meters) the use of nonlinear gravity compensators with a locally linearized working range becomes very attractive. For example, this may be accomplished by means of specially designed elastomeric [6, 9] or pneumatic devices [10].

A relatively new development in such vibration isolation devices for heavy platforms is the electromagnetic vibration

Table 1: Design specifications for the isolation system for high-precision applications.

Property	Requirement
Degrees of freedom	6
Number of actuators	6
Gravity compensation	Passive, magnetic
Passive force level	$7.1\,\mathrm{kN}$
Active force level	$< 70\,\mathrm{N}$
Stroke length	$\pm 1\,\mathrm{mm}$
Positioning	$< 10\,\mu\mathrm{m}$
Isolated mass	$730\,\mathrm{kg}$
Resonance frequency	$< 1\,\mathrm{Hz}$
Damping	Low

isolation system with passive magnetic, or contactless, gravity compensation. In such a system a permanent magnet based gravity compensator exhibits a passive vertical force that lifts a platform. It is assisted by active actuators which ensure stabilization and advanced vibration isolation. Such system exhibits a high vibration isolation bandwidth, low energy consumption and low noise injection compared to commercially available systems. The main design challenge for such a device is to combine low stiffness with a large gravity compensation force. Table 1 summarizes the requirements that have been defined for the gravity compensator under focus. Especially the combination of a large passive vertical force, a small active force and small stroke require that the modeling technique that is used to design this device must be very precise.

A Surface charge modeling

The analytical surface charge modeling technique is considered very suitable to obtain the 3D magnetic fields and interactions of permanent magnets in free space. These methods provide a fully 3D computation of the field, without a need for meshing. As such, they are extremely precise - especially at large magnetic field gradients - and time inexpensive field calculation, especially compared to numerical methods [11]. Its mesh-free properties further eliminate the necessity for model boundaries; neither periodicity, iron boundaries or limited solution space are required, nor is the total considered volume of influence on the computational efforts of these models. This enables the analysis of non-repetitive structures or structures with strong end-effects.

The resulting analytical models tend to be very fast, accurate and provide great insight into the parametric properties. Their linearity enables the use of superposition to model the force between magnets with any magnetization direction. They are especially suitable for ironless applications with permanent magnets, such as magnetic couplings [12], Lorentz actuators [4, 5, 13], planar actuators [14] or passive high-field magnetic cavities [15] although simple iron boundaries may be incorporated by means of the method of imaging [16]. Superposition is suitable to model magnets with a magnetization vector which is not exactly along one of the Cartesian coordinate vectors.

This analytical modeling technique is based on the scalar potential formulation $-\nabla \Psi = \vec{H}$ under the assumptions that the relative permeability $\mu_r = 1$ and a current-free region by $\nabla \times \vec{H} = 0$. If the magnetization vector $\vec{M}$ is confined to the magnet volume V with surface S, and falls abruptly to zero
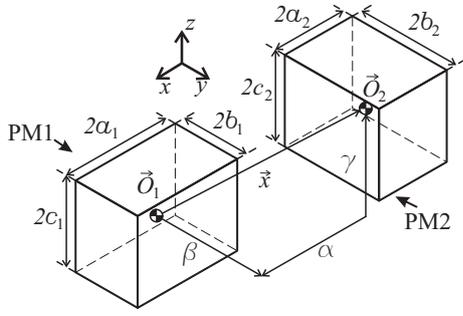
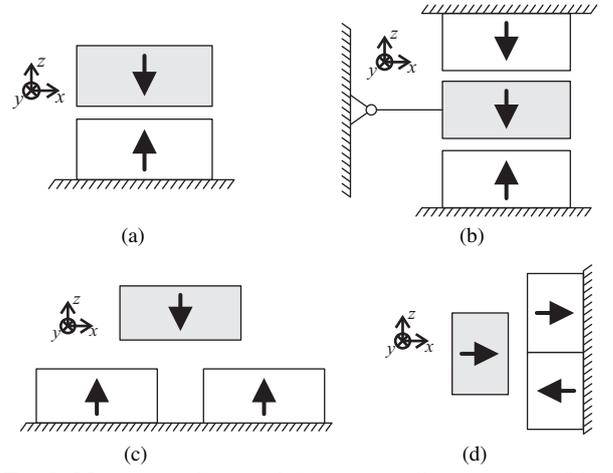Fig. 2: Variable definition for two cuboidal magnets in the charge model.

Fig. 3: Magnet topology with (a) two repelling magnets, (b) a combination of repulsion and attraction in two parallel horizontal airgaps (c) unequal magnets and (d) vertical airgaps. The floating magnets are colored grey.

outside this volume, this vector potential becomes [17]

$$\Psi = \frac{1}{4\pi} \int_V \frac{\rho_m(\vec{x}')}{|\vec{x} - \vec{x}'|} \, \mathrm{d}v' + \frac{1}{4\pi} \int_S \frac{\sigma_m(\vec{x}')}{|\vec{x} - \vec{x}'|} \, \mathrm{d}s' \qquad (1)$$

$$\rho_m = \nabla \cdot \vec{M} \, [\mathrm{A/m^2}] \qquad (2)$$

$$\sigma_m = \vec{M} \cdot \hat{n} \, [\mathrm{A/m}] \qquad (3)$$

If the magnetization of the permanent magnet is homogeneous within the magnet, the volume charge density ρ_m is zero and only a surface charge density σ_m remains. The magnetic flux density is written as

$$\vec{B}(\vec{x}) = \frac{\mu_0}{4\pi} \int_S \frac{\sigma_m(\vec{x}')(\vec{x} - \vec{x}')}{|\vec{x} - \vec{x}'|^3} \, \mathrm{d}\vec{s}' \qquad (4)$$

The resulting equations model the permanent magnet as an equivalent distribution of magnetic charges on the side surfaces of its volume.

The exact analytical 3D field equations for cuboidal permanent magnets based on the aforementioned method were introduced in [18]. For example, the field of the first magnet PM1 in Fig. 2 with a remanent flux density B_r in the z-direction is given by

$$\vec{B}(\vec{x}) = \frac{B_r}{4\pi} \sum_{i=0}^{1} \sum_{k=0}^{1} \sum_{p=0}^{1} (-1)^{i+k+p} \begin{pmatrix} \log(R-T) \\ \log(R-S) \\ \mathrm{atan}\left(\frac{ST}{RU}\right) \end{pmatrix} \qquad (5)$$

$$S = x - (-1)^i a_1 \qquad (6)$$

$$T = y - (-1)^k b_1 \qquad (7)$$

$$U = z - (-1)^p c_1 \qquad (8)$$

$$R = \sqrt{S^2 + T^2 + U^2} \qquad (9)$$

where the vector $[x; y; z]^T$ is the observation point. If this point is somewhere on the second magnet PM2 it is possible to find an analytical description of their interaction. Various publications have built on these field equations to find closed-form descriptions of the interaction between permanent magnets. The virtual work principle was used to obtain force equations for parallel and perpendicular magnetized permanent magnets in [18] and [19], respectively. Similar equations in in [20] and [21] have been derived using the Lorentz force and produce the same outcome. These force equations take a form which is similar to that in (5)

$$\vec{F}(\vec{x}) = \frac{B_{r_1} B_{r_2}}{4\pi \mu_0} \sum_{i \cdots n = 0}^{1} (-1)^{i+j+k+l+m+n} \vec{\xi}(u, v, w) \qquad (10)$$

Comparable to (5), the vector $\vec{\xi}$ consists of analytical equations that only depend on the respective magnet dimensions and their

relative displacement and is given for the described situations in [18, 19, 20, 21]. A direct analytical description of the position dependency, or stiffness, of this force is given in [22]. These have a similar form to (10). The same holds for the torque equations for parallel magnetized magnets [23, 24] and perpendicular magnetized magnets [25, 26].

B   Passive gravity compensator

As mentioned, the accurate and mesh-free analytical modeling technique is very suitable for modeling non-periodical devices which use the force between permanent magnets. Therefore, it has been employed in the design of the 6-DoF gravity compensator. One of the main challenges in the design of this device is the combination of a high force density with a very low stiffness or displacement dependency according Table 1. The force between two permanent magnets, as shown in Fig. 3(a), has an inverse-exponential relationship with the distance between them [27, 28]. As a result, a reduction of this airgap causes an increase in interaction force, however it simultaneously increases stiffness and as such the resonance frequency. A number of configurations may be applied to reduce this position dependency. In the topology shown in Fig. 3(b) the middle, floating, permanent magnet is repelled by the bottom one (positive stiffness) and is attracted by the top one (negative stiffness). The resulting cancelation of these stiffness values was used in [29, 30] to obtain a low-stiffness gravity compensator, although with limited force capabilities. The use of unequally sized magnets as shown in Fig. 3(c) allows for a reduction in stiffness especially at low airgap lengths [27, 31]. The gravity compensator that is described in this article is based on the vertical-airgap topology that is shown in Fig. 3(d). The floating permanent magnet is repelled by the bottom magnet and attracted by the top magnet, similar to Fig. 3(b). However, the airgap is here vertical which allows for a device which exhibits low stiffness over a larger displacement compared to horizontal airgaps as the magnet's edges are located in a region which has low field gradients [27].

Although vertical displacements hardly have an effect on the force, the topology in Fig. 3(d) is sensitive to horizontal displacements; a reduced airgap causes an increased force amplitude, according [27, 28]. This is solved by introducing symmetry as shown in Fig. 4(a). For example, a movement of the grey floating magnets into the positive x-direction leads to
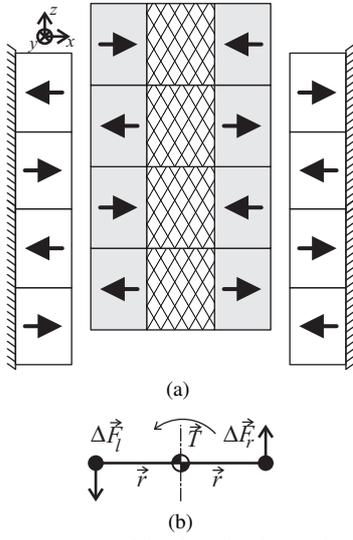
Fig. 4: (a) the symmetrical back-to-back topology and (b) the change in the net force on both sides if the grey floating magnets are moved to the right.
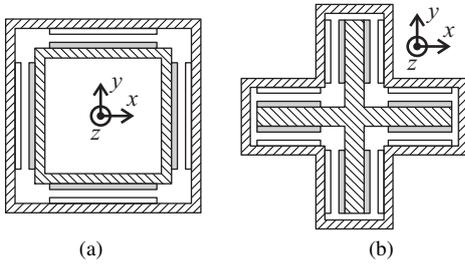

Fig. 5: Top view of a magnetic gravity compensator with vertical airgaps in (a) a square topology and (b) a cross-shaped topology.
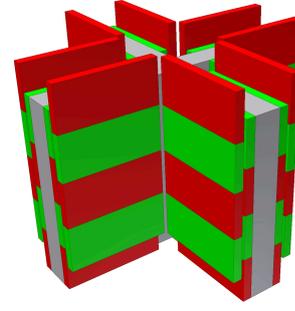

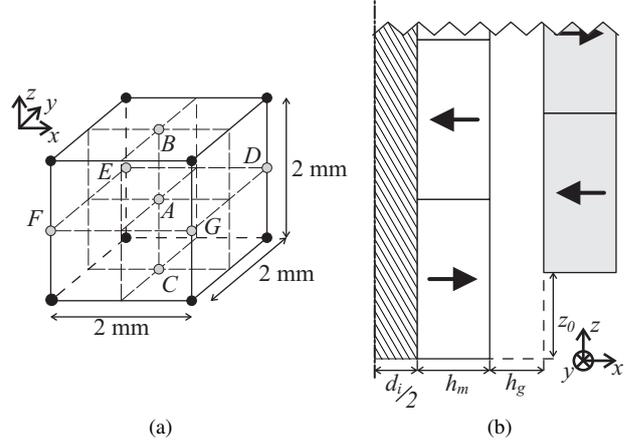Fig. 6: 3D impression of the magnetic topology of the gravity compensator.

Fig. 7: The optimization has been performed on (a) several points from a volume around the working point A for (b) a number of dimensional variables.

a simultaneous increase of force on the right hand side and an almost equal decrease on the left hand side. As Fig. 4(b) shows, both dynamic forces cancel. However, this figure shows too that a torque T around the center of the device is the result of these two dynamic forces. This is summarized as

$$\Delta \vec{F}_l \approx -\Delta \vec{F}_r \qquad (11)$$

$$\vec{T} = 2\vec{r} \times \left(|\Delta \vec{F}_r| + |\Delta \vec{F}_l| \right) \qquad (12)$$

A minimization of this parasitic torque $\vec{T}$ is difficult to be accomplished by a reduction $\Delta \vec{F}$ and therefore the arm r is minimized instead. For this reason, the - intuitive - square topology of Fig. 5(a) is sub-optimal as the arm r, given by the distance between the opposing airgaps, is rather large. For this reason, the cross-shaped topology shown in Fig. 5(b) has been chosen for this gravity compensator [32]. It combines the high force density and low stiffness of the vertical-airgap topology in Fig. 3(d) with the low parasitic torque that results from a minimized distance between opposing magnet arrays from Fig. 5(b). A 3D impression of the magnet topology is shown in Fig. 6.

C   Topology optimization

As a result of their inverse-quadratic force versus displacement properties, permanent-magnet based devices behave inherently nonlinear with respect to displacements. However, it is necessary that their position dependency is low throughout the device's working envelope and not only in the working point of Fig. 5(b). Figure 7(a) shows this working envelope that has been studied: point A is the center of the working envelope cube

that has sides of $2\,\mathrm{mm}$. Points B and C represent a vertical movement, along z, of $1\,\mathrm{mm}$ in each direction. The points D, E. F and G represent a displacement in the horizontal plane at $z = 0$.

A constrained nonlinear multi-variable optimization function has been employed to search for a suitable topology for the magnetic gravity compensator. Some of the main prerequisites for this optimization are summarized in Table 2. The total width of the magnetic topology is limited to $280\,\mathrm{mm}$ and the height of the individual arrays is limited to $160\,\mathrm{mm}$. Each of these 16 arrays consists of four full-pitch magnets with a magnetization according Fig. 4(a). Hence, there is total amount of 64 magnets present in the device as shown in Fig. 6. The dimensions that have been optimized are the magnet width w_m, the magnet thickness h_m, the airgap length h_g, the vertical offset z_0 and the thickness of the inner support d_i. These variables are shown in Fig. 7. The optimization function aims to maintain a vertical force of $7.1\,\mathrm{kN}$ in point A of Fig. 7(a) and minimizes its position dependency throughout the working envelope by evaluating the total force in the other points too [1].

Figure 8 shows the simulation results for the gravity compensator design that have resulted after the optimization procedure. The colored planes represent the vertical position along z from $z = -1\,\mathrm{mm}$ (red) to $z = +1\,\mathrm{mm}$ (yellow). Each plane is simulated for a displacement along x and y. As such, Point A in Fig. 7 corresponds to $x = y = 0$ for the plane $z = 0$ in Fig. 8. As Fig. 8(a) shows the vertical force $F_z = 7.5$ kN remains virtually constant throughout the working envelope. The horizontal force component in Fig. 8(b) equals $F_x = 0$ for $x = 0$ and it varies with a magnitude that is comparable to that of F_z. The remaining force component, stiffness components and torque components are not shown here although they have been obtained with the analytical modeling method.

Table 2: Key dimensions of the gravity compensator.

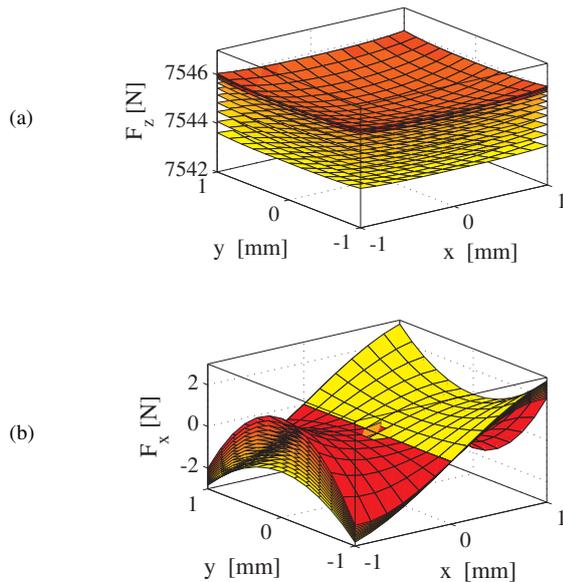| Description	Variable	Value
Maximum array height	h_{max}	160 mm
Maximum total width	$2r_2$	280 mm
Number of stacked poles		4
Remanent flux density	B_r	1.28 T
Magnet width	w_m	91.1 mm
Magnet thickness	h_m	7.1 mm
Airgap length	h_g	3.4 mm
Vertical offset	z_0	19.5 mm
Inner support	d_i	18.5 mm

(a)

(b)

Fig. 8: Vertical (a) F_z and horizontal (b) F_x force characteristics in the working envelope of the gravity compensator, shown for a number of levitation heights.

(a)

(b)

Fig. 9: The vibration isolation test rig in (a) a schematic free-body diagram and (b) a picture showing the main components of interest.

As discussed in Section A one of the most important modeling assumption in the surface charge model is that the relative permeability, μ_r equals unity. However, even high-grade permanent magnets have a relative permeability that is somewhat higher. This issue mainly manifests itself in the vertical offset force as this is a passive force with high magnitude. Therefore, the influence of this assumption has been investigated using a 3D FEM model of the optimized topology [1]. From the results it is concluded that the decrease in force is several percents.

D Experimental verification

The gravity compensator has been validated in a custom test rig which is schematically shown in Fig. 9(a) and the realized system in Fig. 9(b). The gravity compensator supports a granite table of 730 kg. As a permanent-magnet based device is unstable by nature according Earnshaw's theorem [33], the system is stabilized by three 2-DoF external actuation units. These are ironless voice-coil actuators with a quasi-Halbach magnetization [13]. As a result of the extremely low stiffness of the gravity compensator it suffices to stabilize this device with a limited force. A more detailed description of the placement of the various components in the system is found in [1, 34]. A transformation matrix is used to translate the six external actuator positions to three forces and three torques. By means
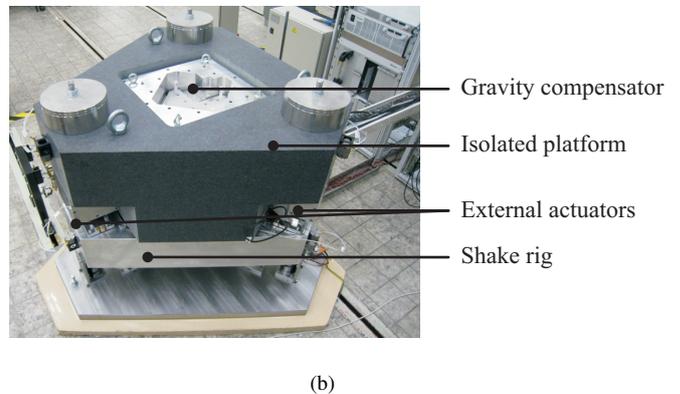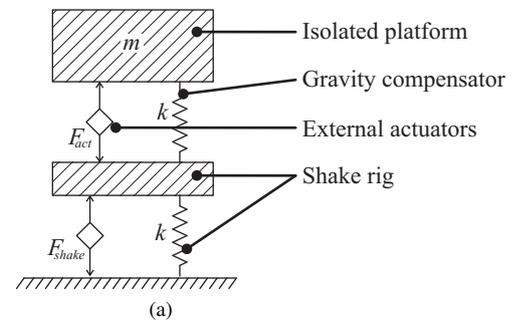
of six independent PID controllers the system is stabilized. As a result of the low stiffness of the device the power consumption remains low; a power between 0.3 W and 0.6 W is required for stable levitation throughout the measured working range.

The validation of the gravity compensator has been conducted indirectly; The external actuators in the test rig have been calibrated with a known mass and have subsequently been used to characterize the device by measuring the mean actuator current that is necessary to stabilize the gravity compensator in a certain position. Figure 10(a) and 10(b) show the F_z and F_x force components that have been measured in the experimental setup, respectively. Measurements of F_y and the torque $\vec{T}$ have been conducted too, however, are not shown here.

The measured vertical force is the force that is generated by the external actuators and, therefore, the gravity force of the isolated platform, which is compensated by the gravity compensator, is absent in this figure. Therefore, it does not have the offset of 7.1 kN that corresponds to the mass of 730 kg that is isolated. Although it is somewhat dependent on displacements along x and y, this vertical force is almost independent on displacements along z as the three measured surfaces are very close together. The horizontal force component F_x shows almost no sensitivity to displacements along y and z, however, does depend on x according $\partial F_x / \partial x \approx -60 \, \text{N/mm}$. A similar instability is seen for $\partial F_y / \partial y$. It is not exactly known what causes these discrepancies, as most modeling and manufacturing inaccuracies only effect the vertical offset force [1] and further research on this subject is necessary. However, it is suspected that reluctance force between the stainless-steel coil bodies of the external actuators and the high-grade permanent magnets in these actuators is the cause of this. Additional measurements need to be conducted to validate this.
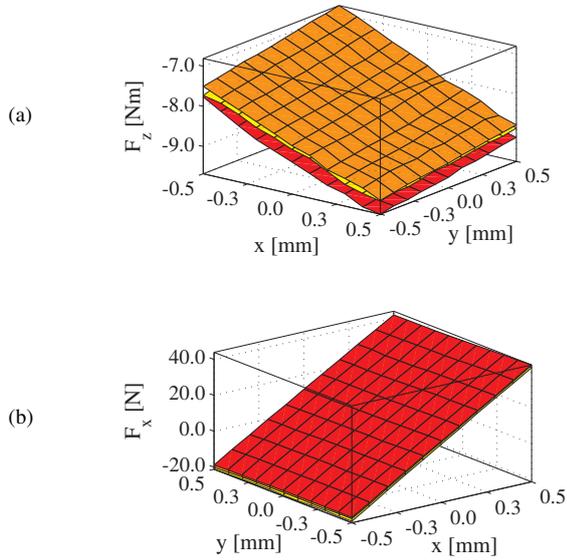
Fig. 10: The measured force components $[F_z, F_x]$. The measured planes are at $z = -0.5\,\mathrm{mm}$, $z = 0.0\,\mathrm{mm}$ and $z = 0.5\,\mathrm{mm}$.

E   Discussion

This research case has shown the potential of the analytical surface charge modeling technique for advanced permanent-magnet based devices. It is a powerful, mesh-free and fast modeling method that can be used to rapidly evaluate magnetic fields or the interaction between permanent magnets. Its high model precision renders it very suitable for applications with extreme demands, such as the 6-DoF gravity compensator discussed above, which has no periodicity and is designed with a large offset force of $7.1\,\mathrm{kN}$ compared to its control margin of less than $60\,\mathrm{N}$. The main modeling assumption that μ_r equals unity mainly leads to a reduction in the vertical offset force, which can be modeled using other modeling techniques such as FEM and therefore can be anticipated on. The gravity compensator has been validated in a test rig, in which it has been shown that a non-complex control structure is sufficient to stabilize the system. The low forces that are related to this confirm the validity of the analytical surface charge model that has been used. Some discrepancies in the horizontal force components are still an open issue as the exact cause of them yet needs to be identified.

IV   CASE B: ELECTROMAGNETIC SUSPENSION SYSTEM FOR AUTOMOTIVE APPLICATIONS

Every form of transportation using a rolling tire requires the carrier to be suspended. The function of a suspension system is three-fold. Firstly, a suspension system fixes the location of the wheel axle in lateral and longitudinal direction. Secondly, it provides a better wheel to road contact since the wheels become independent of each other and have the possibility to follow an imperfect road profile, assuring stability and control. Thirdly, it isolates the driver, passenger, cargo and vehicle from the road disturbances, assuring a comfortable drive, even for the vehicle, increasing its durability. Depending on the functionality, suspension systems can generally be classified as passive, semi-active or active.

All passive suspension systems nowadays consist of a coil spring and a hydraulic or pneumatic damper. The spring

allows for a relative movement between the wheel axle and the sprung mass while providing gravity compensation. The damper absorbs the kinetic energy and reduces oscillatory behavior. A comfortable suspension requires soft springs and a long suspension travel while a good handling performance requires the springs to be stiffer to reduce excessive roll and pitch behavior. Although these passive suspensions are simple, economic and fail-safe, their characteristics are fixed and designers still struggle to find the perfect compromise between a comfortable ride and sufficient handling.

Semi-active or adaptive damping suspension systems appeared around 1980 and have the ability to alter the damping characteristic with minimal amount of energy. Semi-active suspension systems can be hydraulic based, in which the orifice opening is varied to alter the damping behavior [Knutson1991]. Alternatively, they can be based on magnetorheological fluid, in which a magnetic field varies the viscosity of the hydraulic fluid mixed with ferromagnetic particles, again altering the damping characteristic [35]. Although semi-active suspension systems already improve the degree of flexibility and hence performance, they cannot cover the total force-velocity diagram.

Active suspension systems are able to supply energy to the system, and hence deliver high active forces, even in the direction of the velocity and at very low velocities. This allows for both roll and pitch control, leveling and the ability to completely absorb road vibrations. However, the main disadvantage of an active suspension system is the increase in energy consumption. Especially with the introduction of the electric vehicle, energy consumption becomes a major issue [36]. Furthermore, for electric vehicles with in-wheel motors, the unsprung mass increases which leads to a decrease in comfort and active suspension might become necessary to provide a sufficient level of comfort combined with a good handling.

Electromagnetic active suspension systems are becoming increasingly attractive replacements for currently installed passive, semi-active and hydraulic active suspension systems due to their efficiency and decreasing costs [37, 38]. However, their limited force density compared to hydraulic actuators has to be overcome by using advanced electromagnetic modeling to allow for a proper design using optimization and selection of materials. Even more, the ability of regeneration, although limited, make these systems more suitable due to the importance of reduced CO2 emissions. Due to the development towards (hybrid) electrical vehicles, electromagnetic suspension systems are easier to implement since these vehicles their own energy storage system which controls the peak power demand and regenerative power of the active suspension system [39]. Finally, these systems offer an increased bandwidth (100 Hz) relative to hydraulics and pneumatics (5 Hz) which drastically improves the performance with regard to comfort, stability and flexibility of full vehicle control.

The considered system in this paper is a fast direct-drive electromagnetic active suspension system including fail-safe damping by means of eddy currents [40, 38]. The topology consists of a coil spring to provide levitation of the sprung mass. Alternatively, this passive gravity compensation can be solved using permanent magnets as shown in [41, 42, 43], however the total volume of the system is not yet suitable for automotive applications. A direct-drive electromagnetic tubular permanent magnet actuator is placed in parallel with the mechanical spring, converting electrical energy to kinetic energy and providing vertical forces without the need for a gearbox. This process is reversible; hence the kinetic energy can

Table 3: Typical requirements for an automotive active suspension system.

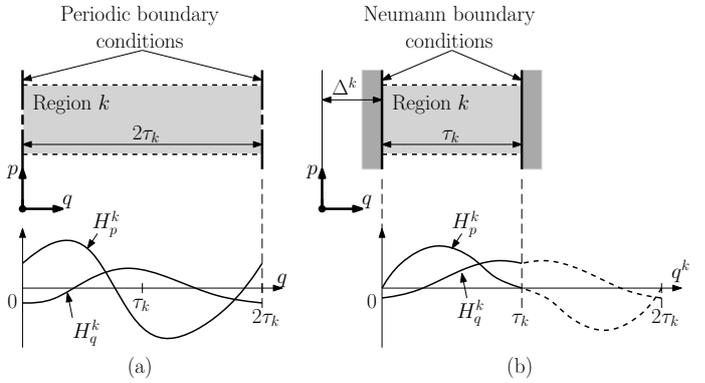| Property	Requirement
Degrees of freedom	7
Number of actuators	4
Gravity compensation	mechanical
Active force level	1 kN
Stroke length	centimeters
Positioning	millimeters
Isolated mass	hundreds of kilograms
Resonance frequency	$\pm$ 1 hertz and $\pm$ 10 hertz
Damping	high at low frequencies, low at high frequencies

Fig. 11: Different types of regions for the harmonic modeling technique, (a) a periodic region and (b) a non-periodic region.

be converted into electrical energy, hereby increasing the total efficiency of the system. Furthermore, passive electromagnetic damping is integrated to make the total system fail-safe [2]. In case a power breakdown occurs, the active suspension behaves as a passive suspension system.

As a comparison to the high-precision application given in Section III, the typical requirements for an automotive vibration isolation system are listed in Table 3. The integrated damping should be sufficient enough to dampen out the sprung mass resonance which is around 1 Hz, but low at higher frequencies to decouple the sprung mass for high frequent disturbances and noise. Considering the total vertical dynamics of a vehicle, the sprung mass has three degrees of freedom (vertical height, roll and pitch angle) and each unsprung mass has its own vertical height, resulting in a total of 7 degrees of freedom. An active suspension system installed at each wheel results in a total of 4 actuators. Hence the system is underactuated and therefore, depending on the road conditions, either comfort (minimizing the vertical acceleration of the sprung mass) or handling (minimizing roll, pitch and/or dynamic tire loads) are emphasized. The electromagnetic active suspension system should inhibit a very high force density (in the order of 755 kN/m^3) with a low power consumption and integrated passive damping to provide a fail-safe functioning.

A Harmonic modeling

To predict the electromagnetic field distributions in long-stroke actuators, the periodicity of the structure can be used to simplify the problem. When end-effects are neglected, the total actuator can be represented by a single periodic section with periodical boundary conditions. In contrast with the previously described surface charge model in Section A, the magnetization is not modeled by equivalent charges, but described as a sum of Fourier series. Since long-stroke actuators generally consists of periodic magnet arrays, this presents an advantage in terms of computation time since the whole magnet array is modeled in once.

The harmonic modeling technique is a method which considers the direct solution of the Maxwell equations using separation of variables. The geometry is therefore divided into separate orthogonal regions such that the boundaries are parallel to one of the directions of the coordinate system. This facilitates the use of separation of variables. For a magnetostatic boundary value problem, the Maxwell equations are written in terms of the magnetic vector potential, $\vec{A}$, where

$$\vec{B} = \nabla \times \vec{A} \qquad (13)$$

with $\vec{B}$ the magnetic flux density. The Maxwell equations are then represented by a Poisson equation, given by

$$\nabla^2 \vec{A} = -\mu_0 \nabla \times \vec{M} - \mu \vec{J} \qquad (14)$$

for a permanent magnetization $\vec{M}$ and current density distribution $\vec{J}$. The solution of the magnetic vector potential for a two-dimensional coordinate system (p, q), which only has a component orthogonal to the p- and q-direction, can then be written as

$$A = \sum_{n=1}^{N} \Big(A_{sn}(p)\sin(w_n q) + A_{cn}(p)\cos(w_n q) \Big) + A_0(p) \qquad (15)$$

with $w_n = \frac{n\pi}{\tau_k}$ and $2\tau_k$ the width of a periodic region, see Fig. 11(a). The functions A_{sn}, A_{cn} and A_0 depend on the type of coordinate system that is considered, Cartesian, polar or axisymmetric. From the magnetic vector potential, the magnetic flux density $\vec{B} = B_p \vec{e}_p + B_q \vec{e}_q$ can be derived using

$$\vec{B} = \nabla \times \vec{A} \qquad (16)$$

According to the location of the sources (permanent magnets or current densities) and the different permeabilities of the materials, the total geometry is divided into regions. Furthermore, for two-dimensional problems, two types of regions can be distinguished. First, regions with periodical boundary conditions in the q-direction (tangential), Fig. 11(a) and second, regions with Neumann boundary conditions in the q-direction (referred as non-periodic regions), Fig. 11(b), can be considered.

Since for a non-periodic region, the magnetic vector potential should be zero on the left and right side of the region, A_{cn} is set to zero for every n and the width of a non-periodic region is defined as τ_k, see Fig. 11(b). As such, boundary value problems including rectangular iron structures can be modeled, such as slotted stators in electrical machines. The iron is however assumed to have an infinite permeability at the sides of a non-periodic region, see Fig. 11(b). The final solution is further obtained by solving a set of boundary conditions which results in a set of algebraic equations solved by matrix inversion [44]. Various types of boundary conditions can be considered for every region

- a continuous boundary condition between two periodic or non-periodic regions,

- a Neumann boundary condition at a single side of a periodic or non-periodic region,

- a Dirichlet boundary condition at a single side of a periodic or non-periodic region,

- a combined continuous and Neumann boundary condition between a periodic or non-periodic regions and a number of non-periodic regions,

- the conservation of flux around a soft-magnetic area surrounded by periodic and non-periodic regions

- Ampère's law applied at the interface between a periodic or non-periodic regions and a number of non-periodic regions.

Applying this set of boundary conditions to a given boundary value problem completely defines the magnetostatic field solution. Because the geometry can be built up of a combination of periodic and non-periodic regions, a large class of electromagnetic problems can be modeled using this technique. Furthermore, the permanent magnets and current sources can be located in any region. Another strong advantage of this method is that every region can have its own finite relative permeability. Therefore, the relative permeability of the permanent magnets is included and even the soft-magnetic material can be incorporated with a finite permeability in case the region is periodic.

The number of harmonics for each region should be chosen carefully, an extensive discussion on the effect of the number of harmonics taken into account is given in [45]. Considering regions with Neumann boundary conditions, the choice of the number of harmonics for these regions should be related to the number of harmonics included in the adjacent regions. To visualize this effect on the accuracy, the field solution due to a single slot opening (non-periodic region) above an airgap and a quasi-Halbach magnet array (periodic regions) is calculated with the analytical model in the axisymmetric coordinate system. The maximum relative error of the field solution in the center of the airgap and inside the slot opening between the analytical and FEA model is shown in Fig. 12 as a function of included harmonics in the periodic regions, N_k, and included harmonics in the non-periodic region, N_j. A trend for the best accuracy is obtained when the number of harmonics in the non-periodic region is given by [2]

$$N_j = \left\lceil \frac{\tau_j}{\tau_k} N_k \right\rceil \qquad (17)$$

which is indicated by the solid line in Fig. 12. A generalized description of this method for 2D electromagnetic problems can be found in [44]. The method is applied to slotted rotary permanent magnet motors in [46, 47], to slotted linear permanent magnet actuators in [48] and to slotted tubular permanent actuators in [49].

Since the advantage in terms of computation time of a 3D (semi-) analytical modeling technique compared to a numerical technique is even more significant, the extension of this technique to 3D problems is even more valuable. Several publications are already considering the harmonic modeling for 3D geometries. Youmssi [50] used the harmonic model to analyze the finite length of a permanent magnet rotor in an electrical machine, and presented an analytical description of the 3D magnetic field distribution in a slotless cylinder. Other examples include the work of Meessen on the 3D effects of segmented cylindrical quasi-Halbach arrays in [51] and the work of Gysen on the 3D modeling of skewed permanent magnet arrays in the cylindrical coordinate system [52]. However, a greater challenge is the incorporation of non-periodic
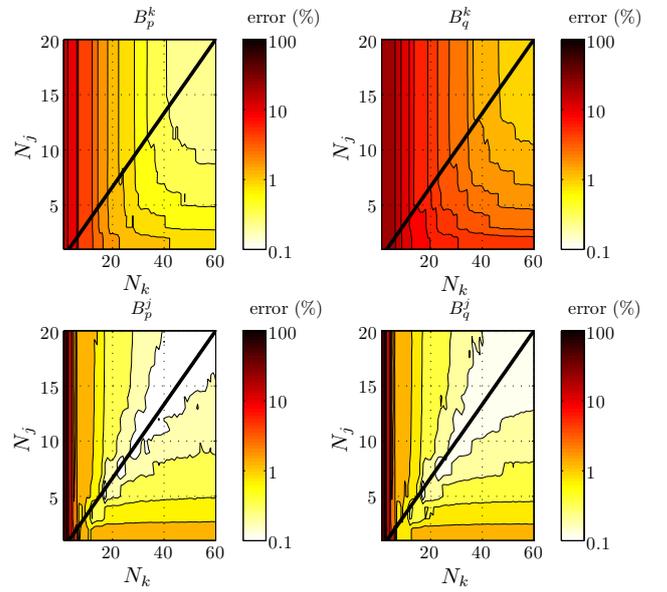

Fig. 12: Error (logarithmic scale) of the normal and tangential flux density in the airgap (B_p^k and B_q^k) and slot opening (B_p^j and B_q^j) related to the included number of airgap (N_k) and slot (N_j) harmonics.
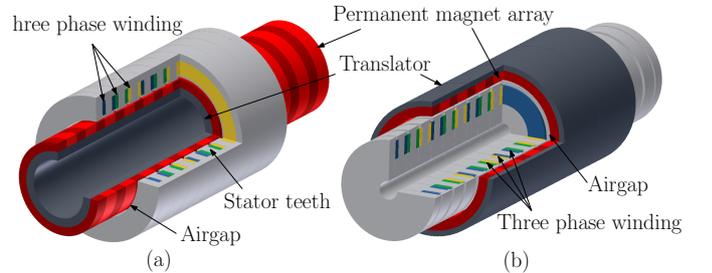

Fig. 13: Tubular permanent magnet actuators, (a) interior magnet topology (IMT) and (b) exterior magnet topology (EMT).

regions surrounded by Neumann boundary conditions. This requires a two-dimensional correlation technique in which numerical implementation becomes a bottleneck. The work of Theodoulidis describes the 3D field solution over a rectangular conductive wedge in Cartesian coordinates, however only a single wedge is considered [53].

B   Direct-drive electromagnetic suspension system

This section describes the developed direct-drive electromagnetic active suspension system. The developed suspension system is a retro-fit for a passenger car, in this case, a BMW530i. Considering the available space envelope for the suspension system, a very high force density, up to 755 kN/m3 is required, providing a nominal force of 1 kN. Additionally, the power consumption of the actuator should be minimized as well as the cogging force since a high force ripple might lead to uncomfortable behavior especially in the passive mode where the actuator cannot compensate for this. The stroke requirement is 140 mm with a maximum velocity of 2 m/s. Considering typical road profiles, only an average velocity of 0.1 m/s is apparent. The passive behavior of the system should perform in a similar manner as the passive BMW suspension system. Hence, the eddy current damping should replace the hydraulic damping and the mechanical coil spring has a similar characteristic as the original coil spring.

Considering the volumetric efficient solution of the coilover

topology, a tubular permanent magnet actuator (TPMA), see Fig. 13, together with a coil spring offers an effective solution of electromagnetic actuation. The coil spring supports the sprung mass while the actuator can provide direct-drive forces in the vertical direction. Due to its cylindrical structure, this technology is more efficient due to the absence of end windings. Additionally, the total magnetic field of the permanent magnets is used for propulsion force due to the axisymmetric structure. Furthermore, it has an ideally zero net attraction force between stator and translator, reducing the friction in the bearings. It consists of a magnet array glued onto a translator and the three phase winding configuration embedded in a slotted stator. When the translator is the inner tube, it is referred as interior magnet topology (IMT), see Fig. 13(a), whereas the exterior magnet topology (EMT) has the stator as inner tube, see Fig. 13(b).

The TPMA is composed of a finite number of periodic sections where each periodic section consists of P number of poles and S number of slots, as shown in Fig. 14. Various magnetization patterns (e.g. radial, quasi-Halbach or axial) or winding configurations can be considered. To apply the harmonic modeling technique, the geometry of this periodic section is divided into regions as: translator support (back-iron or aluminum), magnet array, airgap, slot tip openings and slots. Depending on the type of magnetization, the division of regions differs since a quasi-Halbach array does not require a soft-magnetic back-iron and for axial magnetization the magnet array consists of non-periodic magnet regions separated by pole pieces. When the magnetic flux density distribution in the airgap is obtained, the active force can be calculated by integrating the Maxwell stress tensor over the airgap surface, giving

$$F_{act} = \frac{N_p 2\pi}{\mu} \int_0^{P\tau_p} B_r(r,z)B_z(r,z)r\mathrm{d}z \qquad (18)$$

where N_p is the number of periodic sections and τ_p is the pole pitch. This provides an accurate and fast determination of the force level including the force ripples due to the slotted stator.

Considering the fact that passive damping is desirable, solid steel can be used. Using solid steel enhances the induced eddy currents which is also beneficial from a construction point of view since tubular laminations are difficult and expensive to produce. Although the induced eddy currents in the solid steel provide a certain amount of damping, in general, it is not sufficient to meet the required passive damping which is in the order of 1600 Ns/m. Furthermore, it is desirable to enhance and tune the damping force without significantly altering the actuator design. The slot tip openings in a TPMA are generally filled with a non-magnetic material in order to avoid slot leakage and to provide a finished stator surface. Alternatively, one could use a conductive material like copper or aluminum in order to enhance the induced eddy currents and obtain an increased damping without significantly altering the performance of the actuator [54], see Fig. 14. Furthermore, one can alter the cross section of the conductive rings within the available slot tip opening in order to alter the amount of damping or changing the conductivity by means of choosing the proper material. In this way, the inclusion of damping is obtained without altering the actuator design and increasing the mass [2]. Although a very high damping is desired, the amount of dissipated power is still relatively low due to the low average velocity of the system, $v = 0.1$ m/s. For a given damping ratio of $d = 1600$ Ns/m, the dissipated power is given by
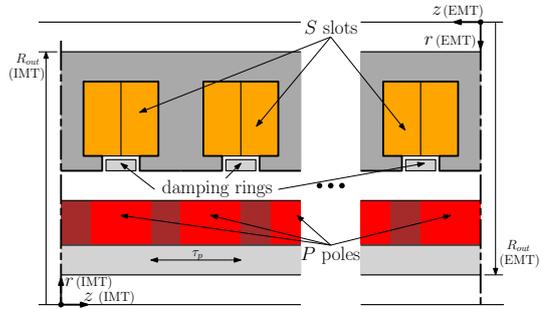
$$P_d = dv^2 \qquad (19)$$

Fig. 14: Cross section of a single periodic section of the TPMA.

which is only 16 W on average. This enhanced damping force can be predicted using the same harmonic modeling technique presented in Section A. Because the magnetostatic field solution is known in any region, the amount of flux linkage due to the permanent magnets linked by the damping rings can be calculated. Furthermore, the inductance of the damping rings can be calculated using the same modeling technique. The resistance together with the inductance determine the impedance of the rings. Using the calculated flux linkage and impedance, the induced eddy currents in the damping rings can be determined. The conductor losses in the damping rings give the amount of dissipated power and resulting damping ratio. This provides a method to design the sizes and select the proper conductive material for these damping rings. A detailed description of the design method can be found in [2].

C Topology optimization

Previous section described how the harmonic modeling technique is applied to model the total magnetic field distribution due to the permanent magnets and armature current. Besides the fact that various magnetization patterns are possible, various winding configuration can be considered as shown in Fig. 15. The concentrated winding configurations, Fig. 15(a) and (b) are characterized by the positive and negative coil of each phase surrounding one tooth. In rotary machines, this topology has the advantage of a short end winding, increasing efficiency, however for tubular actuators, this advantage is not applicable. Due to the nonnecessity of a return coil, the concentrated winding configurations can be transformed into a singular winding configuration as shown in Fig. 15(c) and (d). They achieve the same performance with a $\sqrt{3}$ higher current, but lower total copper loss (75%) since the winding resistance is reduced by a factor four. Furthermore these configurations are easier to manufacture and have a higher total filling factor than the concentrated winding configurations due to absence of the isolation between two coils within one slot. The distributed winding configuration, Fig. 15(e), has a full pitch winding, and therefore a unity winding factor. However, due to the integer slot-pole number, a large cogging force is obtained. The distributed winding configurations shown in Fig. 15(f) and (g) have a high winding factor together with a relatively low cogging force and force ripple. Additionally, the modular winding configuration of Fig. 15(g) has advantages from a construction point of view since the coils of each phase are grouped together [55].

As for the topology optimization of the gravity compensator, a constrained nonlinear optimization routine is used to find the optimal configuration and geometrical sizes providing the necessary force density of 755 kN/m^3. The cost function of the non-linear constrained optimization problem is given by the
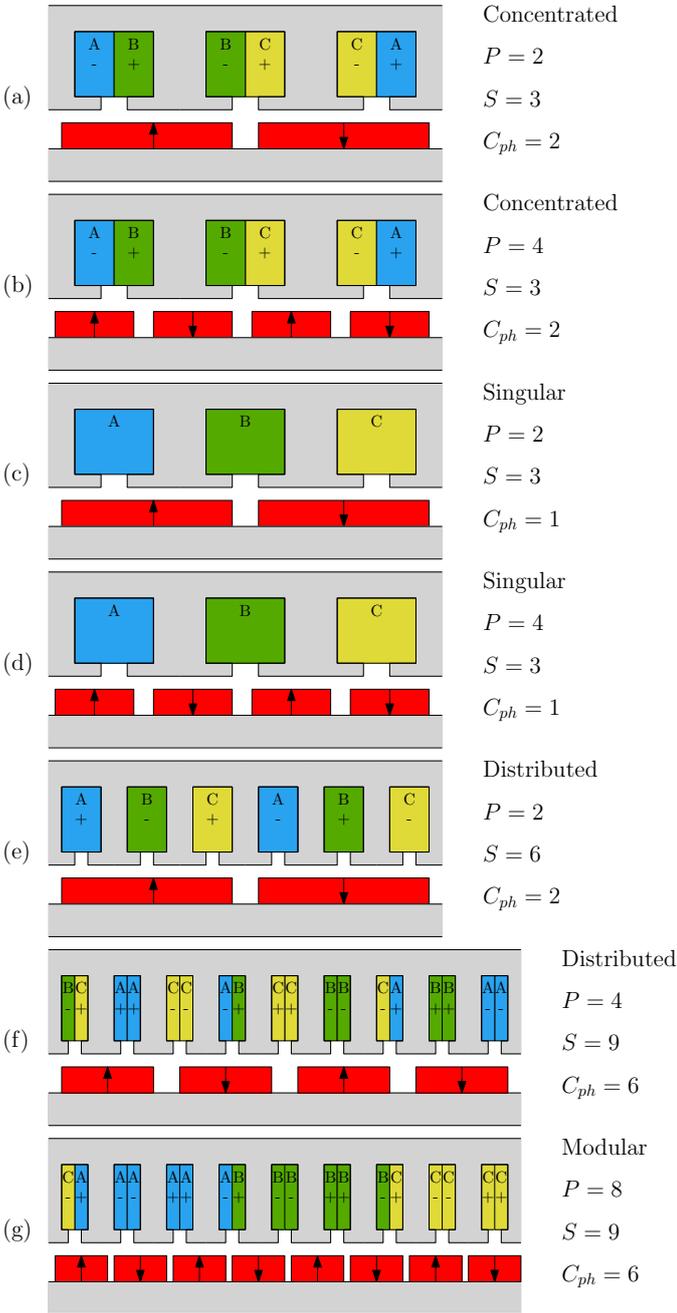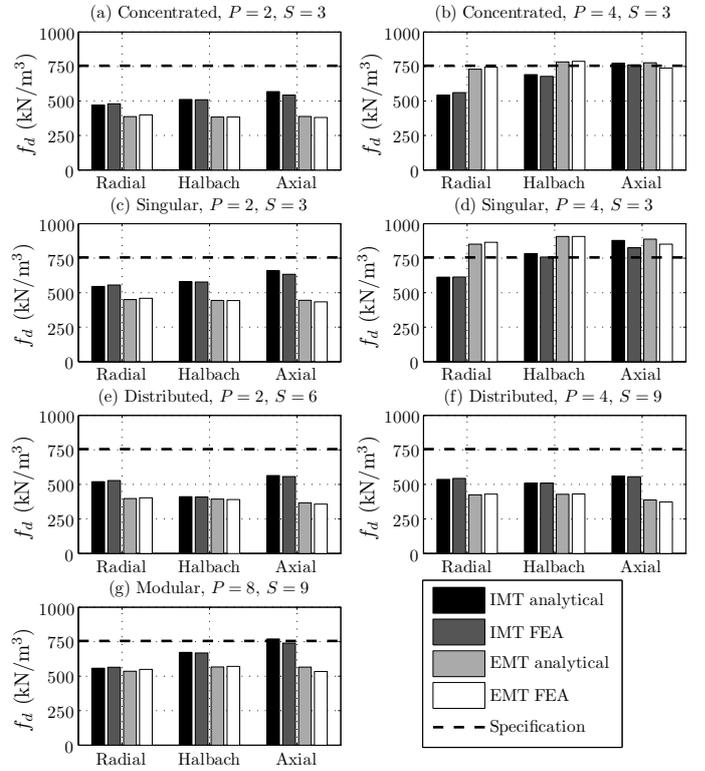
Fig. 15: Considered winding configurations for the TPMA.

Fig. 16: Results of the force density optimization of the various TPMA topologies.

maximization of the force density, hence

$$\mathcal{G}(\vec{x}) = -f_d(\vec{x}) = -\frac{\langle F_{act}(\vec{x}) \rangle}{P \tau_p \pi R_{out}^2} \qquad (20)$$

The various constraints are geometrical limitations, limited flux density in the soft-magnetic material (2.3 T, cobalt iron was chosen as a soft-magnetic material), limited operating temperature (110 °C) and maximum force ripple (10 %).

The optimized force density for each of the topologies is shown in Fig. 16. The highest force densities are obtained using four poles and three slots where a singular winding configuration, Fig. 15(d), is better than a concentrated winding configuration, Fig. 15(b), due to the lower copper losses for an equal electrical loading. For the distributed winding configuration, Fig. 15(e), the force ripple constraint was limiting the optimized performance. The distributed winding configuration, Fig. 15(f), and the modular winding configuration, Fig. 15(g), have a very low force ripple but only the axial IMT topology of the latter configuration is capable of

providing the necessary force density as observed in Fig. 16. The final design is chosen to be the EMT with quasi-Halbach magnetization and a singular winding configuration with four poles per three slots.

Finally, aluminum rings are inserted in the slot openings to obtain a sufficient damping characteristic. Since the rings have a smaller diameter for the EMT, they have a lower resistance and therefore a higher damping ratio can be achieved. More details on the design of the damping rings can be found in [2].

D   Experimental verification

A prototype of the final design is manufactured, see Fig. 17, for experimental verification of the performance of the direct-drive electromagnetic active suspension system. The output force, F_{act}, as a function of the quadrature current, I_q, is shown in Fig. 18 were a linear characteristic up to 2 kN is achieved. The measured damping force and damping ratio due to the induced eddy currents in the solid steel and aluminum damping rings is shown in Fig. 19. A sufficient damping at low velocities of 1450 Ns/m is obtained. The difference between the finite element results and the measurements is accounted for the various slits and holes that had to be made in the stator teeth and the aluminum rings to guide the lead wires.

Consequently, controllers were developed based upon a quarter car representation of the vertical vehicle dynamics. Control of active suspension systems dates back from the 1970's when the computational performance of micro-controllers was developing rapidly. Ever since, numerous papers have been written on the control of active suspension systems. They can be classified according to the applied control strategy. The most commonly used strategies are skyhook [56], optimal control (LQR/LQG) [57], robust control (H_∞ and μ-synthesis) [58], fuzzy logic and adaptive control [59]. In this research, the H_∞ controllers were developed to ensure proper stability and performance for a wide range of variations within
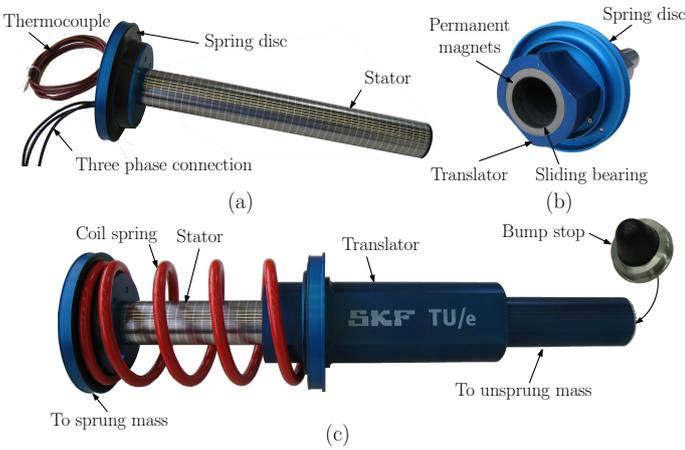
Fig. 17: Prototype of the direct-drive electromagnetic active suspension system, (a) the stator, (b) the translator and (c) the total assembly (Courtesy of TU/e and SKF).
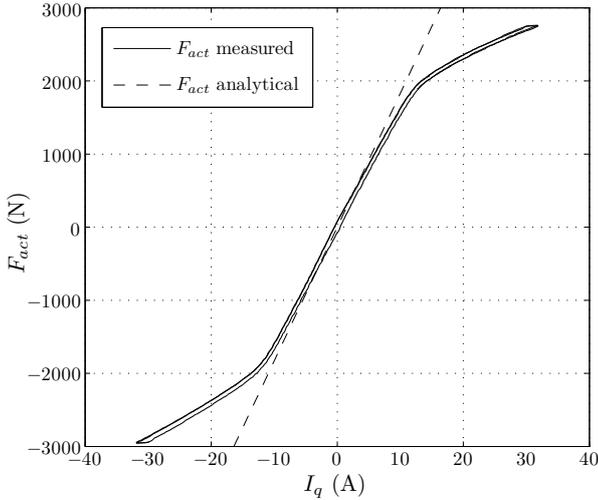

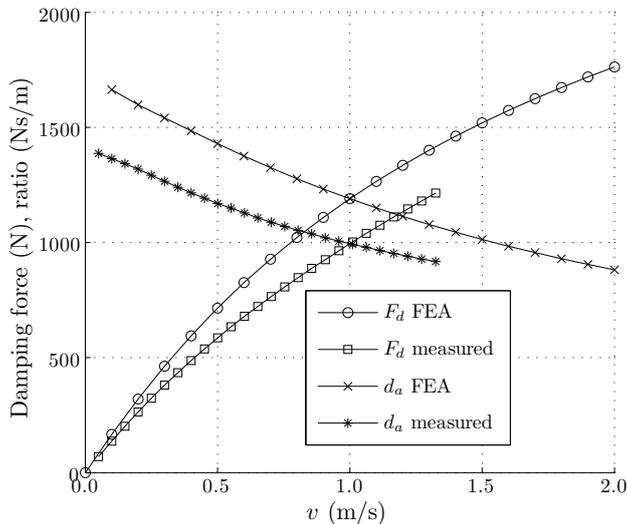Fig. 18: Measured output force as a function of the quadrature current.

Fig. 19: Measured damping force and damping ratio as a function of the velocity.
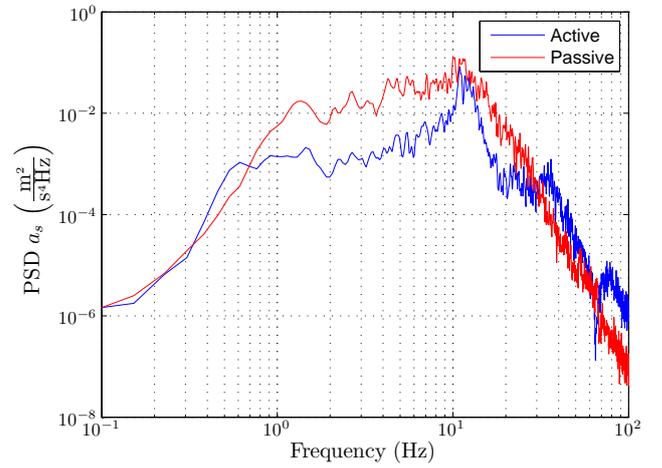

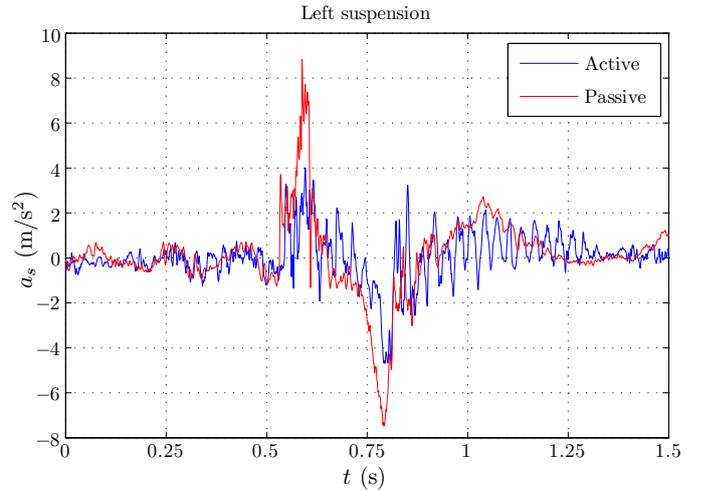Fig. 20: PSD of the measured sprung acceleration on the quarter car test setup for the active and passive case.

Fig. 21: Measured sprung acceleration during a test drive over a speed bump with the passive and active suspension system.

the vehicle. Parameter variations are considered for the sprung mass, tire pressure and damping ratio (due to its nonlinearity and temperature dependency).

Although an H_∞-controller provides more stability and performance with respect to plant or system variations, the actual performance is less compared to an optimal controller for the nominal plant. Furthermore, the variations in inputs (road disturbances and driver inputs) are large and in that respect, it is more beneficial to consider adaptive control to provide a higher level of performance under any conditions. However, this work considers the performance of an H_∞-controller as a benchmark result for future development of control strategies. The sensor inputs for the controller are chosen to be the sprung and unsprung acceleration and the suspension travel, at each corner of the front suspension. A more detailed information on the control design can be found in [2, 60].

To verify the performance of the controlled suspension system, it is installed on a quarter car test setup which simulates the vehicle dynamics of one corner of the car. This setup allows for controlled and reproductive road conditions to make a fair comparison between the passive and active case. The sprung acceleration, a_s, is measured for the active and passive case for rough road conditions and the PSD is shown in Fig. 20. A significant reduction can be seen, especially within the frequency band of 0.5-20 Hz which is the band where humans are most sensitive to vertical vibrations. The power consumption during this test was only 110 W which is significantly less than commercial hydraulic active suspension systems which consume around 500 W per corner.

Finally the active suspension system is installed in the front suspension of a BMW 530i. The first test undertaken is the
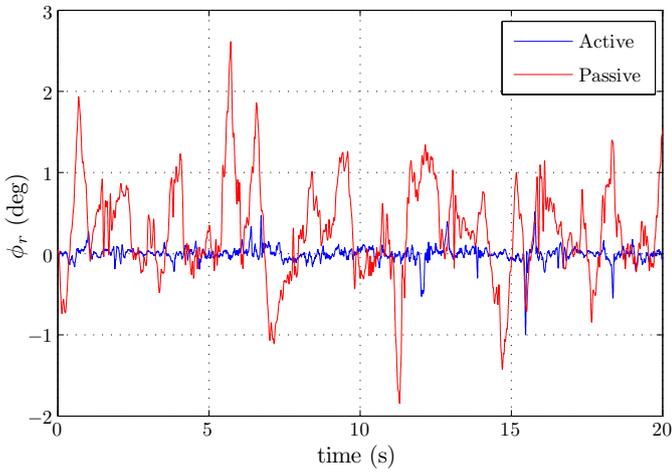
Fig. 22: Measured roll angle during a test drive on the TU/e campus road with the passive and active suspension system.
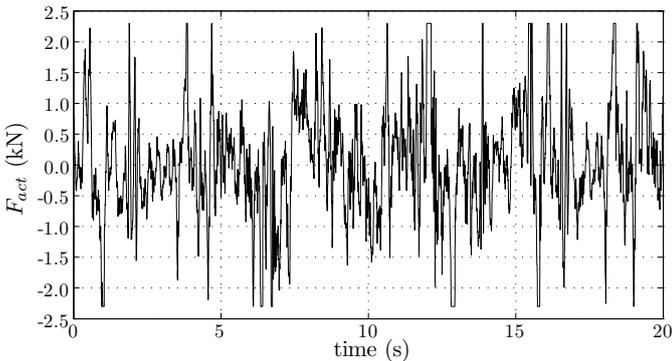

Fig. 23: Applied actuator forces during a test drive on the TU/e campus road.

vehicle driving over a speed bump situated on the left side of the vehicle with 25 km/h. The response of the front left body acceleration for the passive case (fail-safe mode) and the active case are shown in Fig. 21. It can be observed that the peak acceleration is significantly reduced from 9 to 4 m/s². However, an additional resonance is observed for the active case. This resonance can be accounted to the stick-slip friction of the suspension system. This is the major disadvantage and performance limitation of the MacPherson topology in the combination with an active suspension. This could be minimized by considering side-force cancelation using a special coil spring geometry.

The second test is performed while driving on the terrain of the Eindhoven University of Technology (TU/e). The objective of the test is to improve the handling of the BMW 530i. Since this objective requires the highest actuator forces, this test shows the high performance of the active suspension system. However, yaw rate, yaw angle or lateral acceleration could not be measured using the current sensor set on the vehicle. Alternatively, the roll angle in degrees, ϕ_r, is minimized, which is derived using the left and right suspension travel as

$$\phi_r = \frac{180}{\pi} \arctan\left(\frac{\Delta_{zl} - \Delta_{zr}}{T_w}\right) \qquad (21)$$

where T_w is the track width of the vehicle, and Δ_{zl} and Δ_{zr} are the suspension travel of the front left and right corner, respectively. In Fig. 22, the roll angle is shown during the test track for the passive (fail-safe mode) and active case. It can be observed that the roll angle is reduced significantly, from a maximum of 2.65 degrees for the passive case to a maximum

of 1 degree for the active case. The required actuator force is shown in Fig. 23. It should be noted that the maximum force was limited to 2300 N during this test. This control strategy creates a very stiff suspension and the responsiveness of a steering command is improved, as was experienced during driving. However, the stability is reduced after cornering since this the suspension is no longer independent and front traction is reduced, leading to a slight increase in understeer. Although this is by no means an optimized control strategy to improve stability, since only the roll angle is minimized, it still illustrates the high performance and potential of the active suspension system. Future development of efficient full-car control strategies is however still necessary.

E   Discussion

The applicability of the harmonic model to the design of long-stroke actuators has been proven in this case. It allows for the modeling of a broad selection of topologies within a very short computation time. Furthermore, parameter variations have a minimal effect on the accuracy of the method in case the number of harmonics is chosen correctly. Due to the possibility to include non-periodic regions, the applicability of the method is very broad. Therefore, the slotting effect and related cogging force can be predicted accurately. This allows for a minimization of the force ripple during design while optimizing the force density of for example the active suspension system described above. Prototypes of this design have been manufactured and their performance have been experimentally verified during on-road tests. A reduction in body accelerations of around 50% compared to the passive suspension system is achieved. Furthermore, the body roll is reduced from 2.5 to 1 degree during a high speed cornering test.

V   Conclusions

This article has presented the results of two research subjects which incorporate (semi-)analytical modeling applied to the design of electromagnetic vibration isolation systems. The use of electromagnetic devices in such systems is promising in terms of isolation bandwidth and energy consumption, although this technique is not technologically mature yet. The (semi-)analytical electromagnetic models of such devices are very precise and have only low computational requirements, especially compared to numerical methods such as FEA. It is shown that the analytical surface charge model is very suitable for the modeling and design of an ironless magnetic gravity compensator for high-precision applications. The analytical harmonic model is employed for the modeling and design of long-stroke tubular actuators for automotive suspension systems. For both cases, experimental verification is performed on a prototype with excellent agreement compared to the (semi-)analytical predictions. This proves the applicability of these modeling techniques for optimization and design of electromagnetic vibration isolation systems.

REFERENCES

[1] J. L. G. Janssen, "Extended analytical charge modeling for permanent-magnet based devices: Practical application to the interactions in a vibration isolation system," Ph.D. dissertation, Eindhoven University of Technology, 2011.

[2] B. L. J. Gysen, "Generalized harmonic modeling technique for 2D electromagnetic problems: Applied to the design of a direct-drive active suspension system," Ph.D. dissertation, Eindhoven University of Technology, 2011.

[3] K. Hameyer, J. Driessen, H. de Gersem, and R. Belmans, "The classification of couples field problems," *IEEE Transactions on Magnetics*, vol. 35, no. 3, pp. 1618–1621, 1999.

[4] J. M. M. Rovers, J. W. Jansen, and E. A. Lomonova, "Analytical calculation of the force between a rectangular coil and a cuboidal permanent magnet," *IEEE Transactions on Magnetics*, vol. 46, no. 6, pp. 1656 –1659, 2010.

[5] J. W. Jansen, C. M. M. v. Lierop, E. A. Lomonova, and A. J. A. Vandenput, "Modeling of magnetically levitated planar actuators with moving magnets," *IEEE Transactions on Magnetics*, vol. 43, no. 1, pp. 15–25, 2007.

[6] D. B. DeBra, "Vibration isolation of precision machine tools and instruments," *Annals of the CIRP*, vol. 41, no. 2, pp. 711–718, 1992.

[7] E. E. Ungar, D. H. Sturz, and C. H. Amick, "Vibration control design of high technology facilities," *Sound and Vibration*, pp. 20–27, 1990.

[8] H. Amick, M. Gendreau, T. Busch, and C. G. Gordon, "Evolving criteria for research facilities: I - vibration," in *Proceedings of the SPIE Conf.*, vol. 5933, San Diego, California, pp. 302–305, 2005.

[9] R. A. Ibrahim, "Recent advances in nonlinear passive vibration isolation," *Journal of Sound and Vibration*, vol. 314, pp. 371–452, 2008.

[10] M. Heertjes, A. van Engelen, and M. Steinbuch, "Optimized decoupling in active vibration isolation systems," in *5th IFAC Symposium on Mechatronic Systems*, Marriott Boston Cambridge, pp. 293–298, 2010.

[11] L. H. D. Medeiros, G. Reyne, and G. Meunier, "Comparison of global force calculations on permanent magnets," *IEEE Transactions on Magnetics*, vol. 34, no. 5, pp. 3560–3563, 1998.

[12] R. Ravaud, G. Lemarquand, and V. Lemarquand, "Analytical design of permanent magnet radial couplings," *IEEE Transactions on Magnetics*, vol. 46, no. 11, pp. 3860 –3865, 2010.

[13] J. L. G. Janssen, J. J. H. Paulides, and E. Lomonova, "Design of an ironless voice coil actuator with a rectangular coil and quasi-halbach magnetization," in *Proc. on the XV Int. Symp. on Electromagnetic Fields*, Madeira, Portugal, 2011.

[14] J. W. Jansen, J. L. G. Janssen, J. M. M. Rovers, J. J. H. Paulides, and E. A. Lomonova, "(semi-) analytical models for the design of high-precision permanent magnet actuators," *Int. Compumag Soc. Newsletter*, vol. 16, no. 2, pp. 4–17, 2009.

[15] J. M. D. Coey, *Rare-earth iron permanent magnets*, 1st ed. Oxford, UK: Oxford Univ. Press, 1996.

[16] B. Hague, *Electromagnetic Problems in Electrical Engineering*. U.K.: Oxford University Press, 1929.

[17] E. P. Furlani, *Permanent Magnet and Electromechanical Devices: materials, analysis and applications*, 6th ed. London: Academic Press, 2001.

[18] G. Akoun and J. P. Yonnet, "3D analytical calculation of the forces exerted between two cuboidal magnets," *IEEE Transactions on Magnetics*, vol. 20, no. 5, pp. 1962–1964, 1984.

[19] H. Allag and J.-P. Yonnet, "3D analytical calculation of interactions between perpendicularly magnetized magnets: Application to any magnetization direction," *Sensor letters*, vol. 7, no. 4, pp. 486–491, 2009.

[20] F. Bancel, "Magnetic nodes," *J. of Appl. Phys.*, vol. 32, pp. 2155–2161, 1999.

[21] J. L. G. Janssen, J. J. H. Paulides, E. A. Lomonova, F. Bölöni, A. Tounzi, and F. Piriou, "Analytical calculation of interaction force between orthogonally magnetized permanent magnets," *Sensor letters*, vol. 7, no. 3, pp. 442–445, 2009.

[22] J. L. G. Janssen, J. J. H. Paulides, and E. A. Lomonova, "Analytical force and stiffness calculations for magnetic bearings and vibration isolation," in *Computer field models of electromagnetic devices*, 1st ed., ser. Studies in Applied Electromagnetics series, E. Napieralska-Juszczak and S. Wiak, Eds. Amsterdam: IOS press, pp. 502–511, 2010.

[23] J. L. G. Janssen, J. J. H. Paulides, J. C. Compter, and E. A. Lomonova, "Three-dimensional analytical calculation of the torque between permanent magnets in magnetic bearings," *IEEE Transactions on Magnetics*, vol. 46, no. 6, pp. 1748–1751, 2010.

[24] H. Allag and J.-P. Yonnet, "3-D analytical calculation of the torque and force exerted between two cuboidal magnets," *IEEE Transactions on Magnetics*, vol. 45, no. 10, pp. 3969 –3972, 2009.

[25] H. Allag, J.-P. Yonnet, and M. E. H. Latreche, "Analytical calculation of the torque exerted between two perpendicularly magnetized magnets," *J. of Appl. Phys.*, vol. 109, p. 07E701, 2011.

[26] J. L. G. Janssen, J. J. H. Paulides, and E. A. Lomonova, "Analytical calculation of the torque between perpendicular magnetized magnets in magnetic suspensions," *IEEE Transactions on Magnetics*, vol. 47, no. 10, pp. 4286 – 4289, 2011.

[27] J. L. G. Janssen, J. J. H. Paulides, and E. A. Lomonova, "Investigation into magnetic gravity compensation using mathematical abstractions in analytical interaction equations," *Progr. in Electromagn. Res.*, 2011, submitted.

[28] W. S. Robertson, B. Cazzolato, and A. Zander, "A multipole array magnetic spring," *IEEE Transactions on Magnetics*, vol. 41, no. 10, pp. 3826–3828, 2005.

[29] K. Nagaya and M. Sugiura, "A method for obtaining a linear spring for a permanent magnet levitation system using electromagnetic control," *IEEE Transactions on Magnetics*, vol. 31, no. 3, pp. 2332 –2338, 1995.

[30] W. S. Robertson, M. R. F. Kidner, B. S. Cazzolato, and A. C. Zander, "Theoretical design paramenters for a quasi-zero stiffness magnetic spring for vibration isolation," *Journal of Sound and Vibration*, vol. 326, pp. 88–103, 2009.

[31] K. B. Choi, Y. G. Cho, T. Shinshi, and A. Shimokohbe, "Stabilization of one degree-of-freedom control type levitation table with permanent magnet repulsive forces," *Mechatronics*, vol. 13, pp. 587–603, 2003.

[32] J. L. G. Janssen, J. J. H. Paulides, and E. Lomonova, "Vibration isolator," European Patent application no. 11150034.4 - 1264, 2011.

[33] S. Earnshaw, "On the nature of the molecular forces which

regulate the constitution of the luminuferous ether," *Trans. Camb. Phil. Soc.*, vol. VII:1, pp. 97–112, 1839.

[34] C. Ding, J. L. G. Janssen, A. A. H. Damen, and P. P. J. van den Bosch, "Modeling and control of a 6-dof contactless electromagnetic suspension system with passive gravity compensation," in *Proc. of the XIX International Conference on Electrical Machines*, pp. 1–6, 2010.

[35] S. Guo, S. Li, and S. Yang, "Semi-active vehicle suspension systems with magnetorheological dampers," in *IEEE International Conference on Vehicular Electronics and Safety*, Beijing, China, pp. 403–406, 2006.

[36] R. Vos, I. J. M. Besselink, and H. Nijmeijer, "Influence of in-wheel motors on the ride comfort of electric vehicles," in *International Symposium on Advanced Vehicle Control*, Loughborough, United Kingdom, pp. 835–840, 2010.

[37] I. Martins, J. Esteves, G. D. Marques, and F. P. da Silva, "Permanent-magnets linear actuators applicability in automobile active suspensions," *IEEE Transactions on Vehicular Technology*, vol. 55, no. 1, pp. 86–94, 2006.

[38] B. L. J. Gysen, T. P. J. v. d. Sande, J. J. H. Paulides, and E. A. Lomonova, "Efficiency of a regenerative direct-drive electromagnetic active suspension," *IEEE Transactions on Vehicular Technology*, vol. 60, no. 4, pp. 1384–1393, 2011.

[39] M. Montazeri-Gh and M. Soleymani, "Investigation of the energy regeneration of active suspension system in hybrid electric vehicles," *IEEE Transactions on Industrial Electronics*, vol. 57, no. 3, pp. 918–925, 2010.

[40] B. L. J. Gysen, J. J. H. Paulides, J. L. G. Janssen, and E. A. Lomonova, "Active electromagnetic suspension system for improved vehicle dynamics," *IEEE Transactions on Vehicular Technology*, vol. 59, no. 3, pp. 1156–1163, 2010.

[41] L. Encica, "Space-mapping optimization applied to the design of a novel electromagnetic actuator for active suspension," Ph.D. dissertation, Eindhoven University of Technology, 2008.

[42] L. Encica, J. J. H. Paulides, E. A. Lomonova, A. J. A. Vandenput,and B. G. v. Leeuwen, "Spring, assembly of springs, assembly of a spring and a damper, as well as a vehicle comprising a spring," WIPO Patent Application PCT/NL2007/050332, 2007.

[43] L. Encica, J. J. H. Paulides, E. A. Lomonova, A. J. A. Vandenput,and B. G. v. Leeuwen, "Spring, assembly of springs, assembly of a spring and a damper, as well as a vehicle comprising a spring," WIPO Patent Application WO/2008/004871, 2008.

[44] B. L. J. Gysen, K. J. Meessen, J. J. H. Paulides, and E. A. Lomonova, "General formulation of the electromagnetic field distribution in machines and devices using Fourier analysis," *IEEE Transactions on Magnetics*, vol. 46, no. 1, pp. 39–52, 2010.

[45] S. W. Lee, W. R. Jones, and J. J. Campbell, "Convergence of numerical solutions of iris-type discontinuity problems," *Microwave Theory and Techniques, IEEE Transactions on*, vol. 19, no. 6, pp. 528–536, 1971.

[46] Z. Q. Zhu, L. J. Wu, and Z. P. Xia, "An accurate subdomain model for magnetic field computation in slotted surface-mounted permanent-magnet machines," *IEEE Transactions on Magnetics*, vol. 46, no. 4, pp. 1100–1115, 2010.

[47] L. J. Wu, Z. Q. Zhu, D. Staton, M. Popescu, and D. Hawkins, "Subdomain model for predicting armature reaction field of surface-mounted permanent-magnet machines accounting for tooth-tips," *IEEE Transactions on Magnetics*, vol. 47, no. 4, pp. 812–822, 2011.

[48] Z. J. Liu and J. T. Li, "Analytical solution of air-gap field in permanent-magnet motors taking into account the effect of pole transition over slots," *IEEE Transactions on Magnetics*, vol. 43, no. 10, pp. 3872–3883, 2007.

[49] Y. Amara and G. Barakat, "Analytical modeling of magnetic field in surface mounted permanent-magnet tubular linear machines," *IEEE Transactions on Magnetics*, vol. 46, no. 11, pp. 3870–3884, 2010.

[50] A. Youmssi, "A three-dimensional semi-analytical study of the magnetic field excitation in a radial surface permanent-magnet synchronous motor," *IEEE Transactions on Magnetics*, vol. 42, no. 12, pp. 3832–3841, 2006.

[51] K. J. Meessen, B. L. J. Gysen, J. J. H. Paulides, and E. A. Lomonova, "Three-dimensional magnetic field modeling of a cylindrical Halbach array," *IEEE Transactions on Magnetics*, vol. 46, no. 6, pp. 1733–1736, 2010.

[52] B. L. J. Gysen, K. J. Meessen, J. J. H. Paulides, and E. A. Lomonova, "3D analytical and numerical modeling of tubular actuators with skewed permanent magnets," *IEEE Transactions on Magnetics*, vol. 47, no. 9, pp. 2200–2212, 2011.

[53] T. Theodoulidis and J. Bowler, "Interaction of an eddy-current coil with a right-angled conductive wedge," *IEEE Transactions on Magnetics*, vol. 46, no. 4, pp. 1034–1042, 2010.

[54] B. L. J. Gysen, J. J. H. Paulides, E. A. Lomonova, L. Encica, and B. G. v. Leeuwen, "Electromagnetic actuator with integrated passive damper," WIPO Patent Application WO/2010/136049, 2009.

[55] J. Wang and D. Howe, "Tubular modular permanent-magnet machines equipped with quasi-Halbach magnetized magnets-Part I: magnetic field distribution, EMF, and thrust force," *IEEE Transactions on Magnetics*, vol. 41, no. 9, pp. 2470–2478, 2005.

[56] D. Hrovat, "Survey of advanced suspension developments and related optimal control applications," *Automatica*, vol. 33, no. 10, pp. 1781–1817, 1997.

[57] P. Venhovens, "Optimal control of vehicle suspensions," Ph.D. dissertation, Delft University of Technology, 1994.

[58] C. Lauwerys, J. Swevers, and P. Sas, "Robust linear control of an active suspension on a quarter car test-rig," *Control engineering practive*, vol. 13, pp. 577–586, 2005.

[59] J. Cao, H. Liu, P. Li, and D. J. Brown, "State of the art in vehicle active suspension adaptive control systems based on intelligent methodologies," *IEEE Transactions on Intelligent Transportation Systems*, vol. 9, no. 3, pp. 392–405, 2008.

[60] T. P. J. v. d. Sande, B. L. J. Gysen, I. J. M. Besselink, J. J. H. Paulides, E. A. Lomonova, and H. Nijmeijer, "Robust control of a direct-drive electromagnetic active suspension system," in *The 8th International Symposium on Linear Drives for Industry Applications, LDIA 2011*, Eindhoven, The Netherlands, pp. 1–4, 2011.

AUTHORS NAME AND AFFILIATION

J. L. G. Janssen, B. L. J. Gysen, J. J. H. Paulides and E. A. Lomonova
Electromechanics and Power Electronics,
Eindhoven University of Technology,
Den Dolech 2, 5600MB Eindhoven, The Netherlands.
j.l.g.janssen@tue.nl
b.l.j.gysen@tue.nl